Pulsed-Laser Deposited 35 $Bi(Mg_{1/2}Ti_{1/2})O_3$-65 $PbTiO_3$ Thin Films—Part I: Influence of Processing on Composition, Microstructure, and Ferroelectric Hysteresis

Carl Morandi, Jennifer L. Gray, Wes Auker, and Susan Trolier-McKinstry, *Fellow, IEEE*

***Abstract*— 35 $Bi(Mg_{1/2}Ti_{1/2})O_3$ - 65 $PbTiO_3$ (35 BiMT-65 PT) is a potential candidate material for a high-temperature nonvolatile ferroelectric memory. For pulsed-laser deposited 35 BiMT-65 PT films with the perovskite structure, it was found that as the chamber pressure during deposition decreased, the Mg and Pb contents in as-deposited films drop, while the concentration of Bi increases. Concurrently with the change in composition, the remanent polarization P_r increases 64% to ≈21 $\mu C/cm^2$ and the polarization–electric field loops rotated counterclockwise as the deposition pressure increases. Decreasing the seed layer thickness from 36 to 16 nm led to a decrease in P_r to ≈14 $\mu C/cm^2$. Adjusting the target composition allowed the deposition of films which had near-stoichiometric Bi and Mg concentrations, but in all cases, the grown films were lead deficient. These films had remanent polarizations of 18–20 $\mu C/cm^2$. If the lead content of the target was increased too far, the remanent polarization decreased, possibly due to the need to evolve more PbO from defective growth layers. Finally, the deposition rate showed no substantial effect on the film composition, but did have a significant impact on the ferroelectric properties. As the deposition rate decreased, the P_r increased to ≈22 $\mu C/cm^2$ due to enhanced crystalline quality. At laser frequencies of 5 Hz, a Mg-rich pyrochlore phase begins to form and films showed a maximum $P_r \approx 22$ $\mu C/cm^2$. The processing-composition behavior is explained via preferential adsorption of Bi on the A-site, which results in lead vacancies.**

***Index Terms*— A-site deficient perovskite, bismuth magnesium titanate–lead titanate, high-temperature ferroelectric random access memory (FeRAM).**

I. Introduction

SINCE the 1990s, lead zirconate titanate (PZT) has provided a stable platform for the production of nonvolatile ferroelectric random access memory (FeRAM) technology, but new materials are being sought to replace it [1]. Currently, Texas Instruments produces state-of-the-art embedded PZT FeRAM on 130-nm node CMOS, with an operating life of 10 years and 1000 h at 85 °C and 125 °C, respectively [2]. Nonvolatile ferroelectric memories are also available from Cypress, Fujitsu, Rohm, and Matsushita (Panasonic) [3]–[6]. Increasing the operating temperature of FeRAM would extend its utility to harsher environments, including automotive applications. While a significant amount of research is dedicated to the scaling of thin film ferroelectrics for FeRAM [2], [7]–[12], high-temperature functionality of the films has not been explored as extensively. Ultimately, the practical limiting use temperature is a fraction of the Curie temperature (T_c). Films with high Curie temperatures and large switchable polarizations are of potential interest for high-temperature FeRAM.

Eitel *et al.* [13], [14] and Randall *et al.* [15] predicted, based on the Goldschmidt tolerance factor [16], that several Bi-based-$PbTiO_3$ solid solutions should have higher transition temperatures than PZT at the morphotropic phase boundary (MPB). This was confirmed experimentally first for $BiScO_3$-$PbTiO_3$, which acts as a PZT-analog, but with an MPB phase transition temperature ∼100 °C higher than PZT [14], [17]. Subsequently, multiple perovskite systems have been demonstrated to exhibit a T_c higher than that of $PbTiO_3$ over part of the solid solution range [18]–[23].

Stringer *et al.* [21] and Stringer [24] proposed three categories of Bi-based-$PbTiO_3$ solid solutions. Category 1 corresponds to systems similar to PZT, where the maximum transition temperature exists at pure $PbTiO_3$. The third category corresponds to systems similar to $BiFeO_3$ where the maximum in T_c increases with decreasing $PbTiO_3$ concentration due to an enhancement in tetragonality. Finally, the second category has a maximum in T_c between the end members, the origins of which are not yet understood.

The focus in this paper is on a category 2 solid solution system: x $Bi(Mg_{1/2}Ti_{1/2})O_3$ - $(1-x)PbTiO_3$ (BiMT-PT). Fig. 1 shows the phase diagram for the BiMT-PT system. The bulk of the literature has focused on compositions around the MPB. Suchomel and Davies [18] utilized the tolerance factor of the non-$PbTiO_3$ end member of known systems to narrow the predicted region for the MPB location (close to $x =$ 62–64 in BiMT-PT). Randall *et al.* [15] refined the MPB compositional region utilizing piezoelectric (d_{33}), poled permittivity, and X-ray diffraction (XRD) measurements. They found

Manuscript received December 10, 2017; accepted April 3, 2018. Date of publication April 9, 2018; date of current version August 29, 2018. This work was supported by Texas Instruments. *(Corresponding author: Carl Morandi.)*

C. Morandi and S. Trolier-McKinstry are with the Materials Science and Engineering Department and Materials Research Institute, Pennsylvania State University, University Park, PA 16802 USA (e-mail: csm204@psu.edu; set1@psu.edu).

J. L. Gray and W. Auker are with the Materials Characterization Laboratory, Materials Research Institute, Pennsylvania State University, University Park, PA 16802 USA.

This paper has supplementary downloadable material at http://ieeexplore.ieee.org, provided by the authors.

Digital Object Identifier 10.1109/TUFFC.2018.2824979

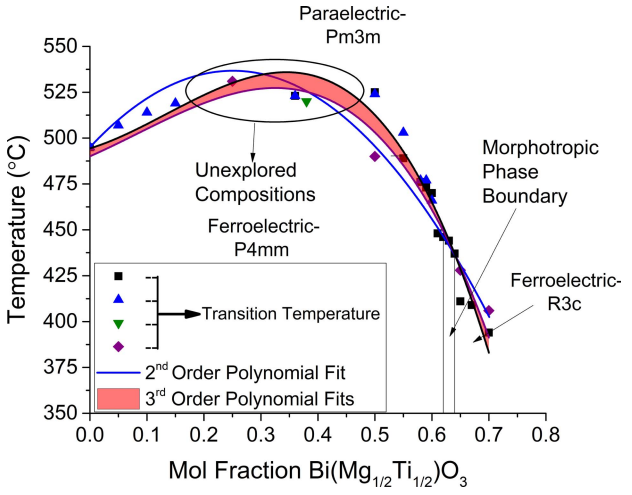

Fig. 1. Phase diagram of the BiMT-PT system. Reported data (blue upward triangle [21], black square [15], purple diamond [18], and green downward triangle [25]) are based on combined high-temperature XRD, differential scanning calorimetry, and dielectric permittivity versus temperature measurements. The blue line corresponds to a second-order polynomial fit as performed by Stringer *et al.* [21], but for all reported data. The shaded region corresponds to third-order polynomial fits and the uncertainty in the transition temperature. See supplemental materials for further details.

that it was hard to pinpoint the exact MPB composition due to the propensity for formation of grains with core–shell structures associated with compositional gradients [15]. BiMT-PT ceramics were reported to have remanent polarizations of ≈33–38 μC/cm^2 (at the MPB of $x = 0.36$ PT) [15], [26] and 25 μC/cm^2 (at $x = 0.5$ PT) [27]. Compositions around the MPB had increased P_r and decreased coercive field E_c and were resistant to thermal depoling to at least 175 °C [26], [28]. Some reports suggest that there is limited domain wall mobility for some BMT-PT with high transition temperatures due to large lattice distortions [26] or defects. In short, BiMT-PT materials demonstrate promise as an alternative high-temperature ferroelectric without requiring use of scandium.

The literature on thin film Bi-based-$PbTiO_3$ solid solutions is considerably smaller than that on bulk ceramics. Zhong *et al.* [42] grew 600-nm 100_c oriented 63 BiMT-37PT thin films with a P_r of 24 μC/cm^2 and a relative permittivity ε_r maximum at ≈415 °C. Zhang *et al.* [28] measured undoped and 0.5-mol% Mn doped 20 BiMT - 80 PT thin films, reporting a stable polarization–electric field response to 125 °C and fatigue resistance up to 10^8 cycles. Oikawa *et al.* [29] and Tanaka *et al.* [30] studied 111_c epitaxial BiMT films, a composition where the perovskite phase is metastable under ambient conditions. Films of Oikawa *et al.* [29] demonstrated little change in P_r over the thickness range of 50–800 nm [30]. Other Bi(Me′ Me″)O_3 - $PbTiO_3$ solid solution thin films have also been produced, including $BiScO_3$-$PbTiO_3$ (BiS-PT) [31], $BiInO_3$ (BiI-PT) [32], [33], $BiAlO_3$-$PbTiO_3$ (BiA-PT) [34], $BiFeO_3$-$PbTiO_3$ (BiF-PT) [35]–[37], and Bi($Zn_{1/2}Zr_{1/2}$)O_3-$PbTiO_3$ (BiZZ-PT) [38]. Of the studied Bi(Me′Me″)O_3-$PbTiO_3$ thin films, BiS-PT, BiMT-PT, and BiI-PT are materials which may be able to withstand harsh environments for actuators, sensors, and FeRAM devices. 0.5-mol% Mn-doped x BiI-(1−x)PT ($x = 0.1$–0.25) exhibit high transition temperatures (558 °C–633 °C) and P_r (25–44 μC/cm^2), but a large frequency dispersion in tan(δ) with temperature from 1 kHz to 1 MHz above 200 °C. 001_c epitaxial 60 $BiScO_3$ −40 $PbTiO_3$ demonstrate a $P_r \approx 42$ μC/cm^2, $\varepsilon_{r,\max}$ at $T \approx 455$ °C, and maintains a low loss (<0.1 at 100 kHz) up to 550 °C [31]. BiA-PT [34], BiZZ-PT [38], and BiMT-PT [39] all demonstrate leakage currents of 10^{-5} A/cm^2 or less at 150 kV/cm, at least an order of magnitude less than that reported for 0.6 $BiFeO_3$ − 0.4 $PbTiO_3$ thin films [35], presumably due to the lower likelihood of electron hopping in the iron-free compositions.

The possibility for BiMT-PT ferroelectrics with large remanent polarizations, a stable high-temperature polarization, and a relatively thickness-independent P_r to film thicknesses of 50 nm are encouraging for developing next-generation high-temperature FeRAM. However, there is still a significant gap in knowledge in the development of BiMT-PT ferroelectrics. As shown in Fig. 1, there is uncertainty in T_c as a function of composition, particularly near $T_{c,\max}$. This is particularly notable for the thin film literature. For example, Liu and Zuo [40], Liu *et al.* [41] reported unseeded and seeded 63 BiMT - 37 PT with $P_r \approx 18$ μC/cm^2 and ≈14–15 μC/cm^2, respectively, but Zhong *et al.* [42] report ≈8 and ≈24 μC/cm^2, respectively, for the same composition. Liu *et al.'s* films show significantly increased leakage compared to those in bulk ceramics [43]. In addition, there are discrepancies between reported film and crystal properties [31], [44]–[48].

This paper investigates a relatively unexplored composition in the BiMT-PT solid solution, with an emphasis on processing–structure–property relationships. In particular, one aspect that has little attention in the literature is the defect chemistry of systems in which both Pb and Bi occupy the A-site of the perovskite lattice, and the role of A-site point defects on electrical properties. Aliovalent point defects in Pb-based perovskites play a significant role in controlling domain wall mobility though V''_{Pb} have been shown to only have a minor influence on the electrical response in PZT [49]. The 35 BiMT - 65 PT was chosen as a model system, as it is near $T_{c,\max}$ in the BiMT-PT system. This paper focuses on the processing-composition-ferroelectric hysteresis response of these materials. A follow-on paper focuses on the thickness dependence of the electrical properties, high-temperature polarization–electric field (P–E) behavior, and charge injection of A-site deficient 35 BiMT - 65 PT thin films [50].

II. Experimental Procedure

The 35 BiMT - 65 PT films were deposited on $PbTiO_3$/Pt/Ti/SiO_2/Si substrates. Either undoped or 5-mol% La-doped $PbTiO_3$ seed layers were deposited on the Pt-coated Si substrates using the sol–gel method to facilitate perovskite nucleation. Lead acetate trihydrate, titanium isopropoxide (97%), lanthanum acetate hydrate, 2-methoxyethanol (2-MOE), and acetylacetone (ACAC) (all from Sigma-Aldrich Inc., St. Louis, MO, USA) were used as raw materials.

TABLE I
LIST OF TARGET COMPOSITIONS INVESTIGATED

Target Name	Pb Excess (mol%)	Bi Excess (mol%)	Mg Excess (mol%)
20Pb10Bi0Mg	20%	10%	0%
30Pb15Bi5Mg	30%	15%	5%
48Pb20Bi10Mg	48%	20%	10%
65Pb20Bi10Mg	65%	20%	10%
85Pb20Bi10Mg	85%	20%	10%

Lead acetate (40-mol% excess) and lanthanum acetate were dissolved in 2-MOE and distilled in a rotary evaporator under Ar gas flow until precipitation. A solution was made by adding titanium isopropoxide and 2-MOE to the precipitated powder with half the molarity of the final solution. After refluxing for 3 h, the solution was distilled, and ACAC (22.5 and 11.25 vol% for a 0.15- and 0.075-M solution, respectively) and 2-MOE was added to reach the final solution molarity. The solution was spun on the substrate at 3000 rpm for 45 s, pyrolyzed at 225 °C and 400 °C for 2 min each, and crystallized at 600 °C under oxygen flow for 1 min. The undoped 0.15-M and a doped 0.075-M solution produced film thicknesses of 36 and 16 nm, respectively.

Ceramic targets with varying compositions were batched using standard ball milling, calcination, and sintering. Briefly, Pb_3O_4, $4MgCO_3Mg(OH)_2.4H_2O$ (40%–43.5% MgO, Alfa Aesar), TiO_2 (cr-el grade, 99.9%, Ishihara Sangyo Kaisha), and Bi_2O_3 (varistor grade, 99.99%, MCP Metal Specialties) were batched in a stoichiometric ratio and balled milled in ethanol for 24 h. After drying at 85 °C, the powder was calcined at 775 °C for 4 h. Varying amounts of Bi_2O_3, PbO (Pb_3O_4 calcined at 700 °C for 1 h), and $MgCO_3$ excesses were added to the stoichiometric batch to compensate for losses during deposition. Table I gives the batched compositions of the targets employed. The powders were vibratory milled for 12 h, dried, pressed into pellets, and sintered at 825 °C for 2–4 h. Ignition losses were taken into account prior to batching.

Pulsed laser deposition (PLD) was used to deposit 35 BiMT - 65 PT films on the seeded substrates. For deposition, the chamber was pumped down to $\approx 10^{-6}$–10^{-7} Torr. A 90%/10% O_2/O_3 mixed gas was employed as the background atmosphere during deposition, with chamber pressures between 60 and 340 mTorr. A KrF excimer laser (Lambda Physik Compex 102, Fort Lauderdale, FL, USA) with an energy density of $\approx 1.6 \pm 0.1$ J/cm^2 was used. The deposition time was 10 min for samples deposited at 10 Hz at 340-mTorr deposition pressure. The laser spot size and laser measured energy are ≈ 11.3 mm^2 and 180 mJ. The deposition time was adjusted to grow films of approximately the same thickness for different processing variables. For samples deposited under different laser deposition frequencies, the number of laser pulses was kept constant. For all samples, the target to substrate distance was maintained at 6 cm and the substrate temperature was maintained at 700 °C. Substrates were bonded to the heater block using silver paste to insure good thermal contact. These parameters were chosen based on conditions for growing BiS-PT and PMN-PT, as well as further optimization [31], [51].

The films' phase purity was studied using a Philips Empyrean X-ray diffractometer with CuKα radiation. Film compositions were determined from focused ion beam milled cross sections using energy dispersive X-ray spectroscopy (EDS) on an FEI Talos transmission electron microscope (TEM) operated at 200 kV in scanning TEM (STEM) mode. High angular dark field (HAADF) images were collected; the resulting image primarily shows mass contrast approximately proportional to the square of the atomic number of the elements present. EDS data were collected using the Bruker Super-X quad X-ray detectors for 5 min with a beam current of approximately 0.25-nA [see supplemental materials (supplemental S.II) for the description of the composition normalization)] EDS quantification was performed using the Bruker Esprit software with the manufacture's supplied sensitivity factors for standardless Cliff–Lorimer quantification. The sensitivity factor database is calculated based on the accelerating voltage used to collect the data and geometry factors of the instrument.

Electrical properties were tested using lithographically defined 75-μm circular Pt top electrodes. The electrodes were deposited in a Lesker CMS-18 sputter tool at an Ar pressure of 2.5 mTorr, and patterned by liftoff. All electrodes were annealed at 600 °C for 1 min in flowing O_2. The thin film ferroelectric properties were studied using a Radiant Precision Multiferroic tester. P–E data were taken at 1 kHz. All positive-up-negative-down (PUND) [10] data were acquired with a 1-ms pulse and 1-ms delays between pulses.

III. RESULTS AND DISCUSSION

In PLD, there are a wide variety of interrelated processing variables that control the plume–substrate interactions, and influence the resulting film structure and properties. To explore this processing space, the substrate temperature was held fixed at 700 °C, the target to substrate distance at 6 cm and the laser fluence at 1.6 ± 0.1 J/cm^2. The deposition pressure, target composition, and laser deposition rate were then varied systematically.

Fig. 2 shows XRD patterns as a function of chamber pressure during deposition, along with a representative TEM cross section showing the elemental map. For all of the processing conditions in this paper, unless stated otherwise, the films are $\{100\}_c$ oriented with a columnar grain structure (see supplemental materials). Additional XRD for other examined processing parameters can be found in the supplemental materials. Fig. 2(a) shows some changes in the shape of the $h00$ family peaks in the XRD patterns as the deposition pressure changes. Given that all of the films are deep in the tetragonal phase field of the BiMT-PT solid solution, these changes were attributed to differences in domain state or a small change in the defect chemistry that influences the lattice parameter. (See supplemental materials for additional information.) Film roughness decreases with lower deposition pressure due to an increase in bombardment energy as

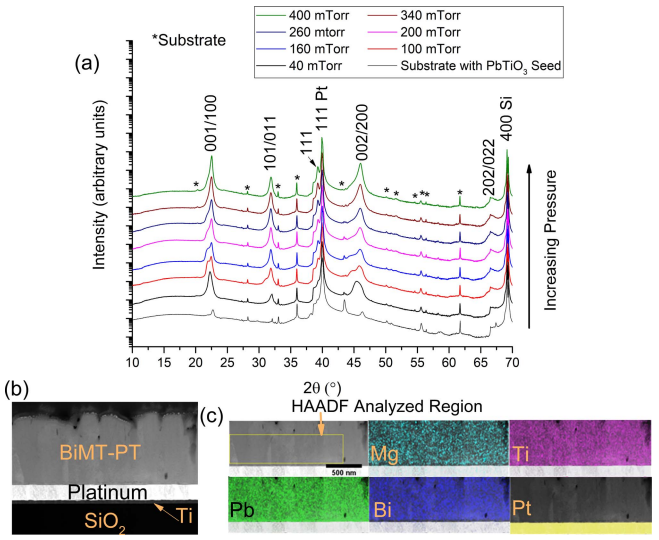

Fig. 2. (a) XRD patterns of films deposited between 40-mTorr and 400-mTorr background pressure. Peaks marked with a star come from the substrate. The film thickness ranged from ≈450 to 900 nm as the deposition pressure increased. Deposition time was 10 min for all samples. (b) and (c) STEM-HAADF image and STEM-HAADF image overlaid with color EDS elemental maps of elements of interest for a film grown at a chamber pressure of 340 mTorr. The thin layer between the Pt and Bi mapping corresponds to the $PbTiO_3$ seed layer.

suggested by the Thornton structure zone mode (see supplemental materials for additional information) [52]. EDS elemental mapping shows the films do not exhibit large spatial elemental segregation.

A. Deposition Pressure-Composition-Ferroelectric Property Relationships

The background chamber pressure controls the mean free path and interaction of ablated species with the background gas, determining the energy and chemical/physical state of species arriving at the substrate surface [53]. In general, high levels of bombardment can cause lattice expansion, imprint formation, and loss of volatile species [54]–[57].

Fig. 3(a) shows the average composition for films deposited between 60 and 340 mTorr. The target utilized had 20-mol% and 10-mol% excess Pb and Bi, respectively. As the deposition pressure decreased, the following phenomena were observed. First, the Mg concentration decreases with decreasing background pressure. The Mg loss is attributed to scattering out of the plume, as it is a light ion. Lichtenwalner [53] demonstrated that the introduction of an ambient gas changes the angular distribution of species ejected from the target. As the chamber pressure is increased, the angular distribution becomes confined. The plume expands at low pressures, and only the central portion of it directly deposits on the substrate. Second, the Pb content also decreases as the chamber pressure drops, presumably as the increased bombardment levels cause more resputtering from the growing film. Finally, the Bi concentration increases as the pressure decreases. This is contrary to what is expected based on its comparatively high propensity for resputtering [56], [57], suggesting that another mechanism must be involved. All films were determined to be

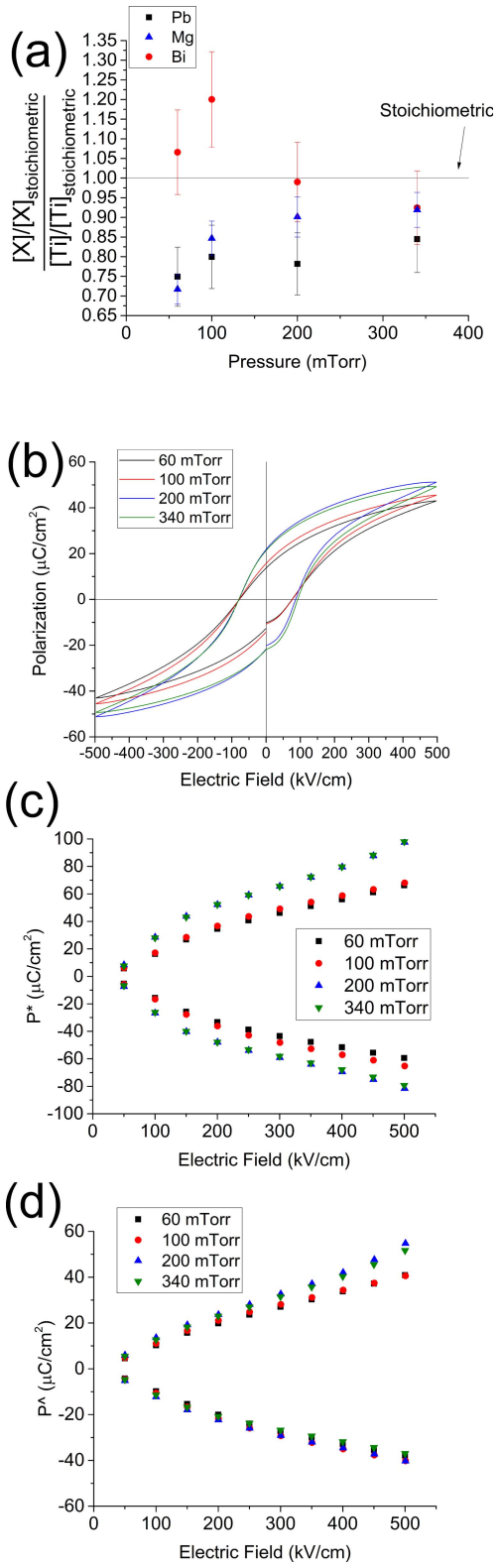

Fig. 3. (a) Concentration of species X, where X is Pb, Mg, or Bi as a function of chamber background pressure. The compositions are normalized to the Ti concentration. A stoichiometric composition would have all cations equal to one. (b) 1-kHz ferroelectric hysteresis response of 670–720-nm-thick films with a 36-nm $PbTiO_3$ seed layer deposited between 60 and 340 mTorr. (c) PUND switching ($P*$) and (d) nonswitching ($P\hat{}$) charge with a 1-ms pulse and 1 ms 0-V holds.

A-site deficient, with a decrease in the overall A-site deficiency as the Bi-concentration increases.

The ferroelectric hysteresis loops shown in Fig. 3(b) for films between 670 and 720 nm in thickness indicate that P_r and maximum polarization (P_{max}) correlate with improved film stoichiometry [Fig. 3(a)]. P_{max}, P_r, and leakage current (see Part II [50]) increase with an increase in background deposition pressure. The increased P_{max} and P_r correlate with a counterclockwise rotation of the P–E loop, resulting in a P_r increase of 64% to 21.3 and −22 μC/cm^2. The correlation between deposition pressure and ferroelectric P–E response may be related to the excess Bi present at lower pressures. Bahri *et al.* [58] and Skanavi *et al.* [59] demonstrated that Bi doping lowers the Curie temperature in $BaTiO_3$. This, in turn, decreases the remanent polarization, as demonstrated by Ogihara *et al.* [60]. The polarization data suggest that the [Bi] strongly influences the P–E response in these films.

PUND measurements were used to quantify total switching (P^*) and nonswitching ($P^\wedge$) charges, respectively, as shown in Fig. 3(c) and (d). With increasing deposition pressure, at 500 kV/cm, the total P^* increases by ≈32 μC/cm^2; however, $P^\wedge$ increases by ≈11–14 μC/cm^2. While other sources may contribute to an increase in $P^\wedge$, the likely source is leakage, given to the relatively small differences in composition and structure from sample to sample. The increase in leakage is expected to be due to A-site vacancy-electron trapping and will be discussed in more detail in a subsequent paper [50].

B. Target Composition-Ferroelectric Property Relationship

A series of targets were made to compensate for the stoichiometric deficiencies in the grown films. Table I lists the batched composition for these targets. If either volatility or resputtering of PbO or Bi_2O_3 is the primary source for the A-site deficiency, then it should be possible to compensate for the nonstoichiometry via the target. A series of films were deposited using each target. All films were deposited at 340 mTorr, a 6-cm target to substrate distance, and a laser deposition rate of 10 Hz. These films were deposited on a 16-nm 5-mol% La-doped $PbTiO_3$ to reduce the influence of the seed layers on the resulting electrical properties. Fig. 4 shows the composition profile and ferroelectric response of the resulting films. Reducing the seed layer thickness resulted in a decrease in P_r to14.4 and −15.2 μC/cm^2 using a 20Pb10Bi0Mg target.

Fig. 4(a) shows that compensation of cation deficiencies is possible for most of the cations. The Bi and Mg compositions approach the ideal concentrations with respect to the Ti concentration on adding 20-mol% and 10-mol% excess, respectively. However, the Pb concentration shows only minor increases regardless of the amount of excess PbO added to the target. It is hypothesized that this may be due to competition between Pb and Bi adsorption onto the A-site.

Fig. 4(b) and (c) shows the ferroelectric response of films deposited from all targets. The control samples deposited from the 20Pb10Bi0Mg target shows the lowest P_r based on P–E (1 kHz) and PUND measurements. As the cation concentration ratios approach ideal, the P_r increases. However, excessive amounts of PbO in the target lead to a decrease in P_r. It is believed that this is a consequence of a greater amount of disorder on the surface associated with the need to evolve more PbO from the surface during growth. The growing layers become more defective and the processing window shifts away from 10 Hz (see Section III-C). Also, the trend in P_r as a function of target composition was not identical to the

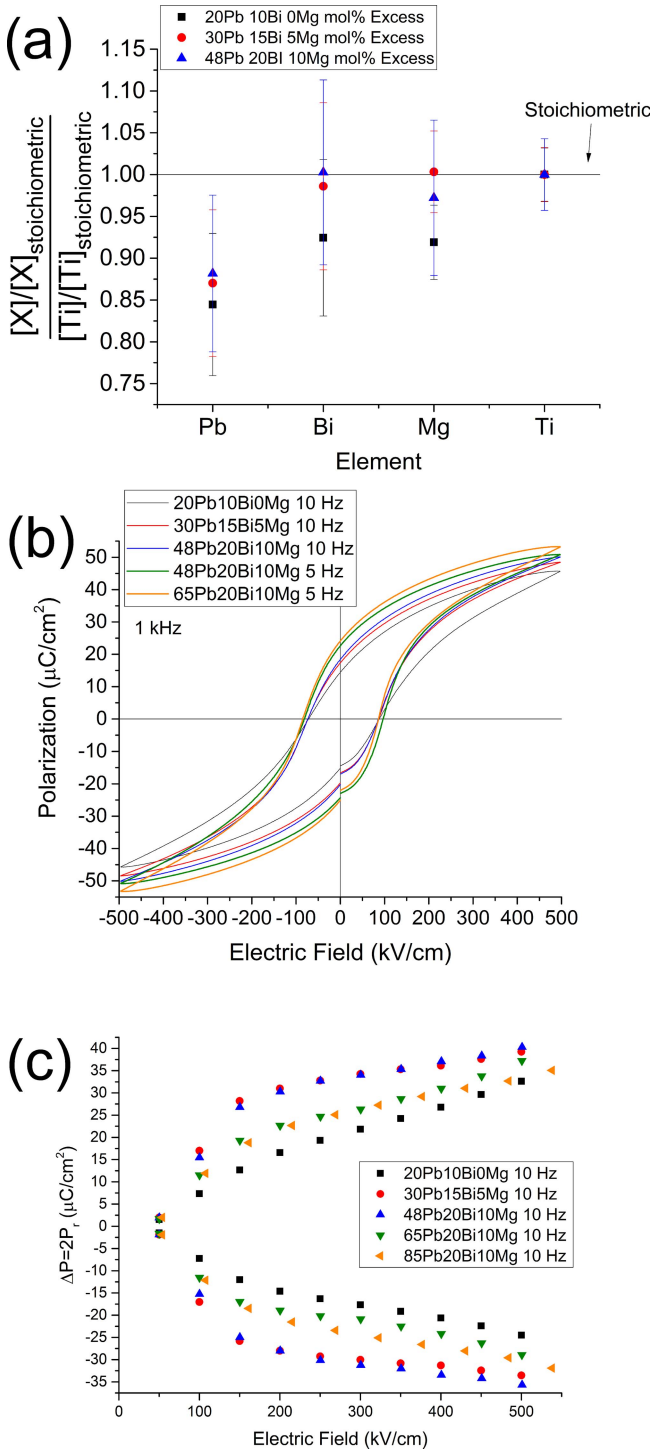

Fig. 4. (a) Normalized composition of 600–700-nm films using a 16-nm (film deposited using a 20 Pb 10 Bi 0Mg target had a 36-nm $PbTiO_3$ seed for composition analysis) $PbTiO_3$ seed layer. The seed layer was avoided during the cross-sectional analysis. (b) Ferroelectric hysteresis (1 kHz) response as a function of target composition (all on 16-nm seed). (c) Sample PUND data for ≈600–700-nm-thick films measured using 1-mS pulses and 1-mS 0-V holds.

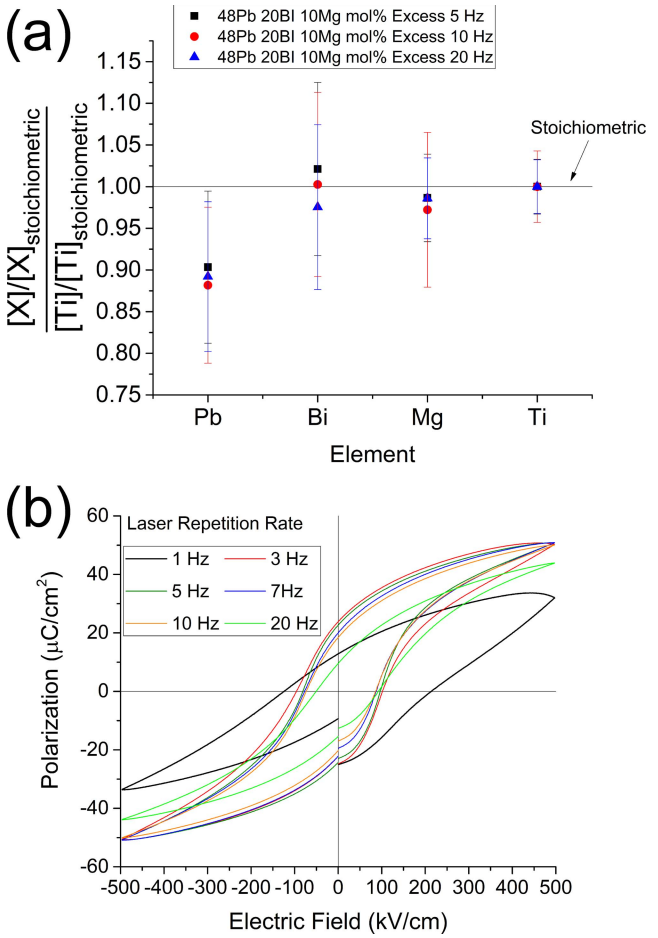

Fig. 5. (a) Composition of films deposited between at laser pulse frequencies of 5–20 Hz. (b) Ferroelectric P–E hysteresis (1 kHz) of films deposited between 1 and 20 Hz.

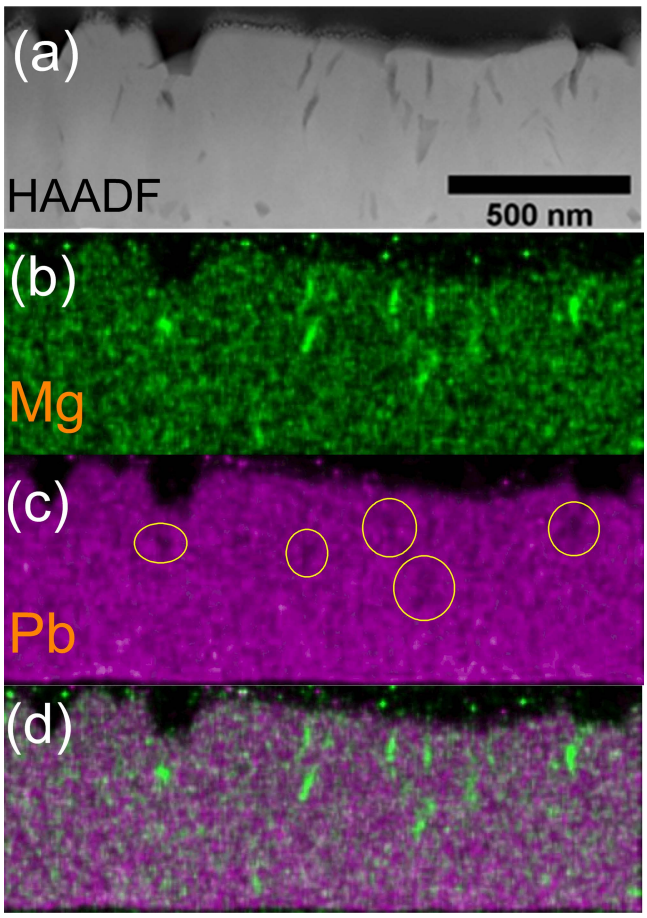

Fig. 6. (a) HAADF-STEM image of cross section from sample from 35 BiMT-65 PT deposited at 5 Hz using a 48Pb20Bi10Mg target at 340 mTorr. Dark regions correspond to a Pb/Bi deficient secondary phase. (b) Mg quantitative EDS elemental map (atomic percentage). (c) Pb quantitative elemental EDS map (atomic percentage). Yellow circles highlight regions with decreased Pb concentrations. (d) Combined Pb and Mg elemental maps showing the overlap between Pb deficient regions and Mg rich regions.

trend in crystallographic orientation as a function of pressure (see supplementary materials for additional details). The mechanism controlling this target composition dependence of P_r is unknown.

C. Laser Deposition Rate-Film Composition-Ferroelectric Property Relationships

The laser repetition rate also influences the film composition. Maria *et al.* [51] and Maria [61] demonstrated for PMN-PT films that lower laser repetition frequencies provide longer times for evolution of the most volatile species. Changing the laser repetition rate leads to a change in the growth rate as well, which can also change the crystalline quality of the resulting films. In particular, slower growth rates are expected to provide more time for atomic rearrangement, leading to improved ferroelectric properties.

Fig. 5 shows film compositions and resulting ferroelectric properties for growth from a 48Pb20Bi10Mg target. It is evident that changing the laser frequency between 5 and 20 Hz does not yield a significant difference in the resulting film compositions. However, there is a significant change in the film properties. The maximum P_r and P_{max} occur at 3 and 5 Hz ($\approx$22 μC/cm^2), while there is a continuous decrease in P_r and P_{max} as the laser frequency increases up to 20 Hz. The loop is noticeably lossier at 3 and 1 Hz. Similar results were found when utilizing targets with greater PbO excess compensation.

Films deposited at frequencies of $\leq$5 Hz contain a Pb deficient and Mg rich second phase (see Fig. 6). Unfortunately, XRD analysis was not sensitive enough to detect secondary phase peaks even in the 1-Hz sample, but the Pb deficiency suggests this is a pyrochlore phase. Interestingly, P_r and P_{max} remain high for the films grown at 5 Hz, regardless of the presence a minor amount of second phase. A similar phenomenon is reported in systems such as PMN-PT [51].

IV. Discussion

The composition of films grown with volatile species can be either flux controlled or adsorption controlled. In flux-controlled growth, the film composition is dependent on the species provided to the growing film. In adsorption-controlled growth, the film composition is dependent on the adsorption kinetics, independent of the species flux. For PLD growth of BMT-PT films under the conditions investigated here, it was found that all films were nonstoichiometric. In particular,

all films were Pb-deficient. Based on the composition data in Figs. 4 and 5, it is clear that a mixture of flux and adsorption control exists in this system. The B-site cations (Mg and Ti) appear to be flux controlled, as adding an excess of Mg leads to an increase in the Mg concentration. However, both A-site cations are adsorption controlled, where Bi adsorption controls the adsorption of Pb into the film. Pb and Bi have been shown to be adsorption controlled in $PbTiO_3$, $Bi_4Ti_3O_{12}$, and other films grown by molecular beam epitaxy [62]–[65].

Fig. 4 demonstrates that Pb is adsorption controlled, as changing the flux of Pb leads to very little overall change in the overall Pb concentration. All films were substoichiometric in Pb. Moreover, the Pb concentration in the film shows far less change than that of Bi with changes in target composition. It is hypothesized that preferential adsorption of Bi in the growing film leads to a fixed concentration of Pb-vacancies, in order to achieve electroneutrality. Considering the chemical formula as $(Bi_{0.35}Pb_{0.65})(Mg_{0.175}Ti_{0.825})O_3$ and the observed defects, several defect reactions may be considered

$$75PbO + 21MgO + 99TiO_2 + 22Bi_2O_3 \xrightarrow{35BiMT-65PT} V''_{Pb} + 2Bi^{\bullet}_{Pb} + 75Pb^{X}_{Pb} + 42Bi^{X}_{Bi} + 99Ti^{X}_{Ti} + 21Mg^{X}_{Mg} + 360O^{X}_{O} \quad (1)$$

$$\frac{1}{2}O_2\,(g) + 25PbO + 7MgO + 33TiO_2 + 7Bi_2O_3 \xrightarrow{35BiMT-65PT} V''_{Pb} + 2h^{\bullet} + 25Pb^{X}_{Pb} + 14Bi^{X}_{Bi} + 33Ti^{X}_{Ti} + 7Mg^{X}_{Mg} + 120O^{X}_{O} \quad (2)$$

$$6MgO + 24PbO + 33TiO_2 + 8Bi_2O_3 \xrightarrow{35BiMT-65PT} V''_{Mg} + 2Bi^{\bullet}_{Pb} + 6Mg^{X}_{Mg} + 24Pb^{X}_{Pb} + 14Bi^{X}_{Bi} + 33Ti^{X}_{Ti} + 1200O^{X}_{O} \quad (3)$$

$$26Pb^{X}_{Pb} + 14Bi^{X}_{Bi} + 7Mg^{X}_{Mg} + 33Ti^{X}_{Ti} + 120O^{X}_{O} \xrightarrow{35BiMT-65PT} V''_{Pb} + V^{\bullet\bullet}_{O} + 25Pb^{X}_{Pb} + 14Bi^{X}_{Bi} + 7Mg^{X}_{Mg} + 33Ti^{X}_{Ti} + 119O^{X}_{O} + PbO(g) \quad (4)$$

and the electroneutrality condition is

$$\left[Bi^{\bullet}_{Pb}\right]2\left[V^{\bullet\bullet}_{O}\right] + p = 2\left[V''_{Pb}\right] + 2\left[V''_{Mg}\right] + n. \quad (5)$$

The lower volatility of Bi, with respect to Pb, is likely to favor excess Bi on Pb sites. Thus, to maintain electroneutrality, $[V''_{Pb}]$, $[V''_{Mg}]$, and/or the electron concentrations will increase. While the dominant defect reaction is not known, all of the films are reasonable insulators at low fields, suggesting that the compensation is predominantly ionic, or that any carriers are in deep traps. The observation of increased leakage currents at high fields does suggest that at least some of the compensation is electronic. In Fig. 3, as the [Mg] and, to a less extent, the [Pb] decrease, there is an increase in the Bi concentration, which is consistent with the defect reactions.

The complex defect chemistry of this system favors non-stoichiometry in films grown by PLD. A-site deficient films grown on $PbTiO_3$ seed layers to stabilize the perovskite phase showed P_r up to 22 μC/cm^2 for films on Si. In contrast, bulk ceramics P_r is reported to be 33–38 μC/cm^2 with similar compositions [15]. The decrease in the P_r with respect to bulk ceramics may be related to a combination of the tensile stress constraining the domain state, and the significant number of point defects in the grown films. More in depth electrical analysis on the electrical response of A-site deficient 35 BiMT - 65 PT thin films is discussed elsewhere [50].

V. Conclusion

≈600–700-nm 35 BiMT-65 PT thin films were deposited using PLD. The film composition was studied as a function of the film deposition pressure, target composition, and laser deposition rate. The processing window for phase pure perovskite 35 BiMT - 65 PT was determined to be very wide in terms of deposition pressure, target composition, and laser deposition rate. EDS measurements showed that the [Mg] and [Pb] decreased with decreasing pressure, while the [Bi] increased. As the film target composition was adjusted, the [Bi] and [Mg] concentrations approached stoichiometric, but the [Pb] remained substoichiometric. Finally, the deposition rate showed no substantial effect on the film composition, but a significant impact on the ferroelectric properties. It was hypothesized that the preferential adsorption of Bi dictates the adsorption of Pb into the A-site. The $2P_r$ increases 64% as the deposition pressure increased and the P–E loops rotated counterclockwise. The P_r increases as the target Pb excess increases to 48 mol%. As the target Pb excess increased over 48 mol%, the P_r decreases possibly due to the need to evolve more PbO from defective growth layers. As the deposition rate decreased, the P_r increased due to enhanced crystalline quality. At laser frequencies of 5 Hz and below, a Mg-rich pyrochlore phase begins to form. A-site deficient 35 BiMT - 65 PT thin films showed a maximum $P_r \approx 22$ μC/cm^2.

Acknowledgment

The authors would like to thank K. R. Udayakumar, J. Rodriguez, and S. Bhaskar at Texas Instruments, Dallas, TX, USA, for their helpful technical discussions.

References

[1] C. Morandi, K. R. Udayakumar, S. Bhaskar, J. Rodriguez, and S. Trolier-McKinstry, "Exploring next generation high temperature ferroelectrics: $35Bi(Mg_{1/2}Ti_{1/2})O_3$ -$65PbTiO_3$ thin films," presented at the IEEE Int. Symp. Appl. Ferroelect. Int. Work. Acoust. Transduction Mater. Devices, and Piezoresponse Force Microsc., 2017.

[2] J. Rodriguez *et al.*, "Reliability of ferroelectric random access memory embedded within 130 nm CMOS," in *Proc. IEEE Reliab. Phys. Symp. (IRPS)*, May 2010, pp. 750–758.

[3] Cypress. *F-RAM (Nonvolatile Ferroelectric RAM)*. Accessed: Sep. 2017. [Online]. Available: http://www.cypress.com/products/f-ram-nonvolatile-ferroelectric-ram

[4] Fujitsu. *Product Lineup*. Accessed: Sep. 2017. [Online]. Available: http://www.fujitsu.com/us/products/devices/semiconductor/memory/fram/lineup/index.html

[5] Rohm and LAPIS Semiconductor Co. *FeRAM*. Accessed: Sep. 2017. [Online]. Available: http://www.lapis-semi.com/en/semicon/memory/feram.html#TabPage1

[6] Matsushita Electric Industry and Panasonic Corporation. *NFC Tag*. Accessed: Sep. 2017. [Online]. Available: http://industrial.panasonic.com/ww/products/semiconductors/nfctags

[7] J. H. Park *et al.*, "Fully logic compatible (1.6V Vcc, 2 additional FRAM masks) highly reliable sub $10F^2$ embedded FRAM with advanced direct via technology and robust 100 nm thick MOCVD PZT technology," in *IEDM Tech. Dig.*, Dec. 2004, pp. 591–594.

[8] D. C. Yoo *et al.*, "Highly reliable 50 nm-thick PZT capacitor and low voltage FRAM device using Ir/$SrRuO_3$/MOCVD PZT capacitor technology," in *Proc. Symp. VLSI Technol.*, Jun. 2005, pp. 148–149.

[9] S. R. Gilbert *et al.*, "Preparation of $Pb(Zr,Ti)O_3$ thin films by metalorganic chemical vapor deposition for low voltage ferroelectric memory," *Appl. Phys.*, vol. 93, no. 3, p. 1713, 2003.

[10] J. A. Rodriguez *et al.*, "Reliability properties of low-voltage ferroelectric capacitors and memory arrays," *IEEE Trans. Device Mater. Rel.*, vol. 4, no. 3, pp. 436–449, Sep. 2004.

[11] K. R. Udayakumar *et al.*, "Low-power ferroelectric random access memory embedded in 180 nm analog friendly CMOS technology," in *Proc. 5th IEEE Int. Memory Workshop (IMW)*, May 2013, pp. 128–131.

[12] B. Prince, "Trends in scaled and nanotechnology memories," in *Proc. Non-Volatile Memory Technol. Symp.*, Nov. 2005, pp. 55–61.

[13] R. E. Eitel, S. J. Zhang, T. R. Shrout, C. A. Randall, and I. Levin, "Phase diagram of the perovskite system (1-x)$BiScO_3$-x$PbTiO_3$," *J. Appl. Phys.*, vol. 96, no. 5, pp. 2828–2831, 2004.

[14] R. E. Eitel, C. A. Randall, T. R. Shrout, P. W. Rehrig, W. Hackenberger, and S.-E. Park, "New high temperature morphotropic phase boundary piezoelectrics based on $Bi(Me)O_3$–$PbTiO_3$ ceramics," *Jpn. J. Appl. Phys.*, vol. 40, no. 10, pp. 5999–6002, 2001.

[15] C. A. Randall, R. Eitel, B. Jones, T. R. Shrout, D. I. Woodward, and I. M. Reaney, "Investigation of a high T_c piezoelectric system: (1-x)$Bi(Mg_{1/2}Ti_{1/2})O_3$–(x)$PbTiO_3$," *J. Appl. Phys.*, vol. 95, no. 7, p. 3633, 2004.

[16] V. M. Goldschmidt, "Die Gesetze der Krystallochemie," *Naturwissenschaften*, vol. 14, no. 21, pp. 477–485, 1926.

[17] R. E. Eitel, C. A. Randall, T. R. Shrout, and S.-E. Park, "Preparation and characterization of high temperature perovskite ferroelectrics in the solid-solution (1-x)$BiScO_{3-x}PbTiO_3$," *Jpn. J. Appl. Phys.*, vol. 41, no. 4A, pp. 2099–2104, 2002.

[18] M. R. Suchomel and P. K. Davies, "Predicting the position of the morphotropic phase boundary in high temperature $PbTiO_3$-$Bi(B'B'')O_3$ based dielectric ceramics," *J. Appl. Phys.*, vol. 96, no. 8, pp. 4405–4410, 2004.

[19] M. R. Suchomel and P. K. Davies, "Enhanced tetragonality in (x)$PbTiO_3$-(1-x)$Bi(Zn_{1/2}Ti_{1/2})O_3$ and related solid solution systems," *Appl. Phys. Lett.*, vol. 86, no. 26, p. 262905, 2005.

[20] D. M. Stein, M. R. Suchomel, and P. K. Davies, "Enhanced tetragonality in (x)$PbTiO_3$-(1-x)$Bi(B'B'')O_3$ systems: $Bi(Zn_{3/4}W_{1/4})O_3$," *Appl. Phys. Lett.*, vol. 89, no. 13, pp. 89–92, 2006.

[21] C. J. Stringer, T. R. Shrout, C. A. Randall, and I. M. Reaney, "Classification of transition temperature behavior in ferroelectric $PbTiO_3$-$Bi(Me'Me'')O_3$ solid solutions," *J. Appl. Phys.*, vol. 99, no. 2, p. 24106, 2006.

[22] S. M. Choi, C. J. Stringer, T. R. Shrout, and C. A. Randall, "Structure and property investigation of a Bi-based perovskite solid solution: (1-x)$Bi(Ni_{1/2}Ti_{1/2})O_3$–x$PbTiO_3$," *J. Appl. Phys.*, vol. 98, no. 3, p. 34108, 2005.

[23] S. Zhang, C. Stringer, R. Xia, S.-M. Choi, C. A. Randall, and T. R. Shrout, "Investigation of bismuth-based perovskite system: (1-x)$Bi(Ni_{2/3}Nb_{1/3})O_3$–x$PbTiO_3$," *J. Appl. Phys.*, vol. 98, no. 3, p. 34103, 2005.

[24] C. J. Stringer, "Structure-property-performance relationships of new high temperature relaxors for capacitor applications," Ph.D. dissertation, Dept. Mater. Sci. Eng., Pennsylvania State Univ., State College, PA, USA, 2006.

[25] J. Liu, X. Chen, G. Xu, D. Yang, Y. Tian, and X. Zhu, "Novel high-temperature ferroelectric single crystals $0.38Bi(Mg_{1/2}Ti_{1/2})O_3$ - $0.62PbTiO_3$ with good and temperature-stable piezoelectric properties," *CrystEngComm*, vol. 17, no. 30, pp. 5605–5608, 2015.

[26] J. Chen, X. Tan, W. Jo, and J. Rödel, "Temperature dependence of piezoelectric properties of high-T_C $Bi(Mg_{1/2}Ti_{1/2})O_3$–$PbTiO_3$," *J. Appl. Phys.*, vol. 106, no. 3, p. 34109, 2009.

[27] S. Sharma and D. A. Hall, "Ferroelectric and antiferroelectric polarisation switching characteristics of $Bi(Mg_{0.5}Ti_{0.5})O_3$-$PbTiO_3$ ceramics," *J. Mater. Sci. Mater. Electron.*, vol. 21, no. 4, pp. 405–409, 2010.

[28] Q. Zhang, Z. Li, F. Li, Z. Xu, and X. Yao, "Temperature dependence of dielectric/piezoelectric properties of (1-x)$Bi(Mg_{1/2}Ti_{1/2})O_3$–x$PbTiO_3$ ceramics with an MPB composition," *J. Amer. Ceram. Soc.*, vol. 93, no. 10, pp. 3330–3334, 2010.

[29] T. Oikawa *et al.*, "Film thickness dependence of ferroelectric properties of (111)-oriented epitaxial $Bi(Mg_{1/2}Ti_{1/2})O_3$ films," *Jpn. J. Appl. Phys.*, vol. 51, no. 9S1, p. 09LA04, 2012.

[30] H. Tanaka, T. Yamada, S. Yasui, K. Yamato, S. Wada, and H. Funakubo, "Growth of (111)-oriented epitaxial $Bi(Mg_{0.5}Ti_{0.5})O_3$ films and their characterization," *Key Eng. Mater.*, vol. 485, pp. 195–198, Jul. 2011.

[31] J. C. Nino and S. Trolier-McKinstry, "Dielectric, ferroelectric, and piezoelectric properties of (001) $BiScO_3$–$PbTiO_3$ epitaxial films near the morphotropic phase boundary," *J. Mater. Res.*, vol. 19, no. 2, pp. 568–572, 2004.

[32] S. Y. Lee, S. W. Ko, S. Lee, and S. Trolier-McKinstry, "Mn-doped $0.15BiInO_3$-$0.85PbTiO_3$ piezoelectric films deposited by pulsed laser deposition," *Appl. Phys. Lett.*, vol. 100, no. 21, p. 212905, 2012.

[33] S. Y. Lee, W. Wang, and S. Trolier-McKinstry, "High Curie temperature $BiInO_3$-$PbTiO_3$ films," *J. Appl. Phys.*, vol. 115, no. 22, p. 224105, 2014.

[34] G. Wu, H. Zhou, X. Zhou, N. Qin, and D. Bao, "Structural, dielectric, and ferroelectric properties of $BiAlO_3$ -$PbTiO_3$ solid solution thin films on indium tin oxide-coated glass substrates," *J. Amer. Ceram. Soc.*, vol. 927, no. 4, pp. 925–927, 2010.

[35] M. A. Khan, T. P. Comyn, and A. J. Bell, "Large remanent polarization in ferroelectric $BiFeO_3$-$PbTiO_3$ thin films on Pt/Si substrates," *Appl. Phys. Lett.*, vol. 91, no. 3, p. 032901, 2007.

[36] M. A. Khan, T. P. Comyn, and A. J. Bell, "Leakage mechanisms in bismuth ferrite-lead titanate thin films on Pt/Si substrates," *Appl. Phys. Lett.*, vol. 92, no. 7, p. 072908, 2008.

[37] M. A. Khan, T. P. Comyn, and A. J. Bell, "Growth and characterization of tetragonal bismuth ferrite–lead titanate thin films," *Acta Mater.*, vol. 56, no. 9, pp. 2110–2118, 2008.

[38] L. Zhang *et al.*, "Large remanent polarization and small leakage in sol-gel derived $Bi(Zn_{1/2}Zr_{1/2})O_3$ -$PbTiO_3$ ferroelectric thin films," *Dalt. Trans.*, vol. 42, no. 2, pp. 585–590, 2013.

[39] L. Zhang *et al.*, "Temperature-independent ferroelectric property and characterization of high-T_c $0.2Bi(Mg_{1/2}Ti_{1/2})O_3$-$0.8PbTiO_3$ thin films," *Appl. Phys. Lett.*, vol. 103, no. 8, p. 082902, 2013.

[40] L. Liu and R. Zuo, "Fabrication and electrical properties of sol-gel derived $0.63Bi(Mg_{1/2}Ti_{1/2})O_3$-$0.37PbTiO_3$ thin films," *J. Amer. Ceram. Soc.*, vol. 94, no. 11, pp. 3686–3689, 2011.

[41] L. Liu, R. Zuo, and Q. Liang, "Effect of $PbTiO_3$ seed layer on the orientation behavior and electrical properties of $Bi(Mg_{1/2}Ti_{1/2})O_3$–$PbTiO_3$ ferroelectric thin films," *Ceram. Int.*, vol. 39, no. 4, pp. 3865–3871, 2013.

[42] C. Zhong, X. Wang, L. Guo, and L. Li, "Characterization of (100)-oriented $0.63BiMg_{1/2}Ti_{1/2}O_3$-$0.37PbTiO_3$ piezoelectric films by a sol-gel process," *Thin Solid Films*, vol. 580, pp. 52–55, Apr. 2015.

[43] L. Liu, R. Zuo, Q. Sun, and Q. Liang, "Structure and electrical properties of Mn doped $Bi(Mg_{1/2}Ti_{1/2})O_3$-$PbTiO_3$ ferroelectric thin films," *Appl. Surf. Sci.*, vol. 268, pp. 327–331, Mar. 2013.

[44] H. Wen, X. Wang, C. Zhong, L. Shu, and L. Li, "Epitaxial growth of sol-gel derived $BiScO_3$-$PbTiO_3$ thin film on Nb-doped $SrTiO_3$ single crystal substrate," *Appl. Phys. Lett.*, vol. 90, no. 20, p. 202902, 2007.

[45] T. Yoshimura and S. Trolier-McKinstry, "Growth and properties of (001) $BiScO_3$-$PbTiO_3$ epitaxial films," *Appl. Phys. Lett.*, vol. 81, no. 11, pp. 2065–2066, 2002.

[46] S. Zhang, C. A. Randall, and T. R. Shrout, "High Curie temperature piezocrystals in the $BiScO_3$-$PbTiO_3$ perovskite system," *Appl. Phys. Lett.*, vol. 83, no. 15, pp. 3150–3152, 2003.

[47] S. J. Zhang, C. A. Randall, and T. R. Shrout, "Electromechanical properties in rhombohedral $BiScO_3$-$PbTiO_3$ single crystals as a function of temperature," *Jpn. J. Appl. Phys. Lett.*, vol. 42, no. 10A, pp. L1152–L1154, 2003.

[48] S. Zhang, C. A. Randall, and T. R. Shrout, "Dielectric, piezoelectric and elastic properties of tetragonal $BiScO_3$-$PbTiO_3$ single crystal with single domain," *Solid State Commun.*, vol. 131, no. 1, pp. 41–45, 2004.

[49] D. M. Marincel *et al.*, "A-site stoichiometry and piezoelectric response in thin film $PbZr_{1-x}Ti_xO_3$," *J. Appl. Phys.*, vol. 117, no. 20, p. 204104, 2015.

[50] C. Morandi and S. Trolier-McKinstry, "35 $Bi(Mg_{1/2}Ti_{1/2})O_3$ -65 $PbTiO_3$ thin films deposited by pulsed laser deposition—Part II: A-site deficiency and thickness scaling influence on electric properties," vol. 65, no. 9, pp. 1534–1541, Sep. 2018.

[51] J. Maria, W. Hackenberger, and S. Trolier-McKinstry, "Phase development and electrical property analysis of pulsed laser deposited $Pb(Mg_{1/3}Nb_{2/3})O_3$–$PbTiO_3$ (70/30) epitaxial thin films," *J. Appl. Phys.*, vol. 84, no. 9, pp. 5147–5154, 1998.

[52] J. A. Thornton, "Structure-zone models of thin films," *Proc. SPIE*, vol. 821, no. 1, pp. 95–105, 1988.

[53] D. J. Lichtenwalner, O. Auciello, R. Dat, and A. I. Kingon, "Investigation of the ablated flux characteristics during pulsed laser ablation deposition of multicomponent oxides," *J. Appl. Phys.*, vol. 74, no. 12, pp. 7497–7505, 1993.

[54] J.-P. Maria, S. Trolier-McKinstry, D. G. Schlom, M. E. Hawley, and G. W. Brown, "The influence of energetic bombardment on the structure and properties of epitaxial $SrRuO_3$ thin films grown by pulsed laser deposition," *J. Appl. Phys.*, vol. 83, no. 8, p. 4373, 1998.
[55] S. B. Krupanidhi, H. Hu, and V. Kumar, "Multi-ion-beam reactive sputter deposition of ferroelectric Pb(Zr,Ti)O_3 thin films," *J. Appl. Phys.*, vol. 71, no. 1, pp. 376–388, 1992.
[56] M. P. Besland *et al.*, "Comparison of lanthanum substituted bismuth titanate (BLT) thin films deposited by sputtering and pulsed laser deposition," *Thin Solid Films*, vol. 495, nos. 1–2, pp. 86–91, 2006.
[57] P. K. Ghosh, A. S. Bhalla, and L. E. Cross, "Surface morphology of R.F. sputtered bismuth titanate thin films," *J. Mater. Sci.*, vol. 29, no. 17, pp. 4659–4662, 1994.
[58] F. Bahri, A. Simon, and H. Khemakhem, "Classical or relaxor ferroelectric behaviour of ceramics with composition $Ba_{1-x}Bi_{2x/3}TiO_3$," *Phys. Status Solidi*, vol. 184, no. 2, pp. 459–464, 2001.
[59] G. I. Skanavi, I. M. Ksendzov, V. A. Trigubenko, and V. G. Prokhvatilov, "Relaxation polarization and losses in nonferroelectric dielectrics with high dielectric constants," *Soviet J. Experim. Theor. Phys.*, vol. 6, no. 2, p. 250, 1958.
[60] H. Ogihara, C. A. Randall, and S. Trolier-McKinstry, "Weakly coupled relaxor behavior of $BaTiO_3$-$BiScO_3$ ceramics," *J. Amer. Ceram. Soc.*, vol. 92, no. 1, pp. 110–118, 2009.
[61] J.-P. Maria, "Epitaxial $Pb(Mg_{1/3}Nb_{2/3})O_3$-$PbTiO_3$ thin films," M.S. thesis, Dept. Mater. Sci. Eng., Pennsylvania State Univ., State College, PA, USA, 1998.
[62] C. D. Theis, J. Yeh, D. G. Schlom, M. E. Hawley, and G. W. Brown, "Adsorption-controlled growth of $PbTiO_3$ by reactive molecular beam epitaxy," *Thin Solid Films*, vol. 325, nos. 1–2, pp. 107–114, 1998.
[63] C. D. Theis *et al.*, "Adsorption-controlled growth of $Bi_4Ti_3O_{12}$ by reactive MBE," *Appl. Phys. Lett.*, vol. 72, no. 22, pp. 2817–2819, 1998.
[64] J. F. Ihlefeld *et al.*, "Adsorption-controlled molecular-beam epitaxial growth of $BiFeO_3$," *Appl. Phys. Lett.*, vol. 91, no. 7, p. 071922, 2007.
[65] J. H. Lee *et al.*, "Adsorption-controlled growth of $BiMnO_3$ films by molecular-beam epitaxy," *Appl. Phys. Lett.*, vol. 96, no. 22, pp. 2008–2011, 2010.

Carl Morandi received the B.Sc. degree in materials science and engineering from the University of North Texas, Denton, TX, USA, in 2011, and the M.S. degree in materials science and engineering from the Pennsylvania State University, State College, PA, USA, in 2014, where he is currently pursuing the Ph.D. degree with the Materials Science and Engineering Department, with a research focus on high temperature ferroelectric thin film processing for ferroelectric random access memory and piezoelectric devices.

Jennifer L. Gray received the B.S. degree in materials science and engineering from the University of Pennsylvania, Philadelphia, PA, USA, the M.S. degree in materials science and engineering from the University of Washington, Seattle, WA, USA, and the Ph.D. degree in materials science and engineering from the University of Virginia, Charlottesville, VA, USA.

She was with Intel as a Process Engineer and a Failure Analysis Engineer, for five years. Her research interests include thin film growth and characterization of semiconductor materials. She is currently a Staff Scientist with the Materials Research Institute, Pennsylvania State University, State College, PA, USA, where she is with the Materials Characterization Laboratory. She works with many research groups using a wide variety of advanced microscopy techniques. Her expertise is in the area of transmission electron microscopy.

Wes Auker received the A.A.S. degree in electronics engineering technology from the Pennsylvania College of Technology, Williamsport, PA, USA, in 2006, and the A.A.S. degree in RF-Communication and fiber optics from the Pennsylvania State University, University Park, PA, USA.

He holds competency credentials/certification in nanofabrication manufacturing technology from the Pennsylvania State University

Susan Trolier-McKinstry (M'92–SM'01–F'09) is the Steward S. Flaschen professor of ceramic science and engineering, a professor of electrical engineering, and the director of nanofabrication facility with the Pennsylvania State University. Her main research interests include thin films for dielectric and piezoelectric applications. She is a fellow of the American Ceramic Society and the Materials Research Society and an Academician of the World Academy of Ceramics. She currently serves as an Associate Editor for *Applied Physics Letters*. She was the President of the IEEE Ultrasonics, Ferroelectrics and Frequency Control Society and Keramos, and the 2017 President of the Materials Research Society. 21 people that she has advised/co-advised have gone on to take faculty positions around the world.